Journal of Electric Propulsion

RESEARCH

Open Access

Validating THz time-domain spectroscopy as a tool for characterizing low pressure inductively coupled plasmas of ion thrusters

Kalle Bräumer[1†], Rodrigo Sandoval Rodriguez[1*†], Markus Stein[1], Konstantin Keil[1], Kristof Holste[1], Felix Becker[1], Jana Zorn[1], Konrad Wehkamp[1], Sangam Chatterjee[1] and Peter J. Klar[1]

†Kalle Bräumer and Rodrigo Sandoval Rodriguez contributed equally to this work.

*Correspondence: rodrigo.ignacio.sandoval.rodriguez@physik.uni-giessen.de

[1] Institute of Experimental Physics I and Center for Materials Research, Justus Liebig University Giessen, Heinrich-Buff-Ring 16, D-35392 Gießen, Hessen, Germany

Abstract

Accurate characterization of plasmas within the discharge chambers of gridded ion engines is essential for their advancement. This study showcases the effectivity of terahertz time-domain spectroscopy (THz-TDS) as a non-invasive technique for profiling low-pressure inductively coupled plasmas, mimicking the conditions of the discharge chamber in a radio-frequency ion thruster. Operating at pressures of $3 - 7 \cdot 10^{-3}$ mbar inside the discharge chamber and a supply power of the radio frequency generator ranging from 10 - 80 W, THz-TDS reveals electron densities in the range of $2 \cdot 10^{16}$ - $2 \cdot 10^{17}$ m^{-3} for xenon, krypton, and argon plasmas. Our results show good agreement with Langmuir probe measurements and global plasma modeling, highlighting the accuracy and reliability of THz-TDS. This validation, conducted under conditions representative of gridded ion engines, demonstrates that THz-TDS is, in principle, suitable for characterizing the electron system of the plasma ignited in such thrusters in operation. This offers great potential of developing a promising additional tool for plasma diagnostics in electric propulsion systems.

Introduction

Electric propulsion systems are increasingly gaining relevance in contemporary space applications due to their wide range of usage, high mass efficiency, and reliability during long operating times [1]. The current development of electric propulsion from a “niche technology” into a commercialized component for space missions faces many challenges and brings exciting opportunities for further development [2].

Among the promising electric propulsion systems are gridded ion engines (GIEs), which offer high mass efficiency, maneuverability, and scalability [2]. Improving the efficiency and thrust of these systems while maintaining their reliability is a primary objective in the field [3, 4].

The main feature of GIEs is the physical separation of the propellant ionisation process and the ion acceleration. In the discharge chamber, a low percentage of the gaseous neutrally charged propellant (such as Xe, Kr, Ar, I_2, etc.) is ionised, and creates a plasma. The charged ions can then be extracted using electric fields applied to the grid system to generate thrust. Electron temperature and charge carrier density are among the most important parameters for characterizing a plasma [5]. They have a decisive influence on the processes taking place inside the plasma such as excitation, ionisation, or dissociation (in the case of molecules), and provide information about the efficiency of the electrical power coupling into the plasma, which is indispensable for ensuring energy-efficient operation, especially in ion engines [2]. Too low electron temperatures push the reaction balance towards excitation processes, which has a negative impact on the ion yield. Too high electron temperatures lead to the formation of multiply charged ions, which reduce the thrust-to-power ratio. In addition, the plasma potential becomes too high, which can lead to undesirable erosion processes inside the discharge vessel and in the extraction grid system [6]. Therefore, to improve GIEs, reliable techniques for characterizing low temperature plasmas and, in case of radio frequency ion thrusters (RITs), inductively coupled plasmas (ICPs) are needed [7].

Up to now, numerous methods have been developed for in situ plasma characterization [8] and are continuously improved. These methods can be broadly classified based on their impact on the plasma during measurement in invasive and non-invasive [9].

Invasive methods such as Langmuir or emissive probes are in direct contact with the plasma. Therefore, they must be designed carefully to minimize their impact on the plasma [8, 10]. Langmuir probes are a commonly used tool for characterizing plasmas and have been the method of choice for many years. Although they have proven their strengths in the field, the analytical process for deriving the plasma parameters is rather intricate and possible sources of error are manifold [11]. Analysing Langmuir probe data often involves the assumption of a Maxwell-Boltzmann distribution for the electron energy distribution function (EEDF) which may not be fully accurate either and can lead to major uncertainties when determining the desired parameters. Furthermore, the characterization of plasmas used within GIEs poses its own challenges. The plasma ignited in the ionisation chamber of the thruster is in most cases inaccessible to electric probes, e.g. Langmuir probes. The wall material, and test conditions either increase the complexity and costs or make it impossible to implement many of the known probe techniques.

Various non-invasive methods such as optical emission spectroscopy (OES) [12], optical absorption spectroscopy, and other laser-based plasma spectroscopy methods have the advantage of a negligible influence on plasma parameters [9], but require a rather complex analysis [13].

The THz-TDS technique utilized in our study is another non-invasive, transmissive measurement technique that provides line averaged plasma parameters [14–16]. However, its distinct advantages lie in its ability to access desired plasma parameters without requiring complex microscopic theoretical models [17, 18].

The plasma frequency of ICPs used in GIEs is in the GHz frequency range. This leads mainly to phase shifts of the interacting broadband THz pulses, a quantity that can be sampled with high precision [19]. THz-TDS provides access to the plasma frequency ω_{p} and thus allows the calculation of the electron density n_{e}. However, the parameters are averaged along the THz line of sight, with the assumption of a uniform electron density and collision frequency distribution along the axis of transmission. These circumstances need to be considered when implementing THz-TDS for characterizing plasmas. As demonstrated by Brown in his dissertation, assuming a uniform distribution yields only a negligible error [20].

Similarly, determining the line-averaged densities inside a GIE offers a measure of the plasma state along the THz line of sight, thereby providing valuable insights into the overall discharge conditions without perturbing the thruster's operation. This approach is particularly beneficial as probes cannot be placed inside the ionisation chamber without risking interference with nominal thruster conditions. The obtained averaged electron densities can be evaluated to analyse trends under variable operating parameters, and direct comparisons with global models allow for model validation and the refinement of theoretical assumptions.

The theoretical limits for characterizing plasmas with THz-TDS have been postulated in another work of Brown et al. [17]. They claim that for a discharge length of 10 cm, electron densities as low as 10^{14} m^{-3} can be measured, depending on the electron collision frequency. This threshold aligns with the conditions that typically prevail in gridded ion engines (GIEs). In the aforementioned study, however, the pressure in the discharge was orders of magnitude higher than that commonly found in GIEs. As a result, Brown et al. only reported electron densities down to $1.4 \cdot 10^{19}$ m^{-3} [17]. While ICPs have been studied using THz-TDS in prior works [15, 17, 21–25], the plasma conditions, particularly in terms of gas pressure, coupling power, and excitation frequency differed significantly from the typical conditions that prevail in GIEs. Notably, Ando et al. applied an approach similar to ours where they compared Langmuir double probe measurements with THz-TDS in an ICP. However, gas pressure and electron densities were magnitudes higher than those found in GIEs [15].

In contrast to previous works, we experimentally demonstrate that THz-TDS can be successfully applied to characterize ICPs at gas pressure regimes and electron densities typically encountered in GIEs. By comparing THz-TDS results with Langmuir double probe measurements and a modified 0D-model based on the work of Chabert et al. [3, 26], we confirm that THz-TDS is ideally suited for analyzing plasmas typical for GIE operating conditions in space. Our proof-of-principle study lays the foundation for employing THz-TDS as a non-invasive characterization tool in the qualification process of GIEs for space flight.

As illustrated in Fig. 1a, our study specifically targets low-pressure ICPs, extending the application of THz-TDS to probe low-density plasmas that have not been previously explored using this technique. These low-pressure plasmas are prevalent within GIEs, and the primary challenge in applying THz-TDS is the reduced electron density, which is directly correlated with the plasma frequency [18]

$$\omega_\mathrm{p} \equiv \sqrt{\frac{n_\mathrm{e} e^2}{\epsilon_0 m}}. \tag{1}$$

Figure 1b shows the line integrated electron densities determined by THz-TDS in previous works on ICPs in comparison with those studied in this work and typical values for ion thrusters. The line integrated densities are obtained by multiplying the local density in the discharge chamber with the plasma length. This is a critical factor

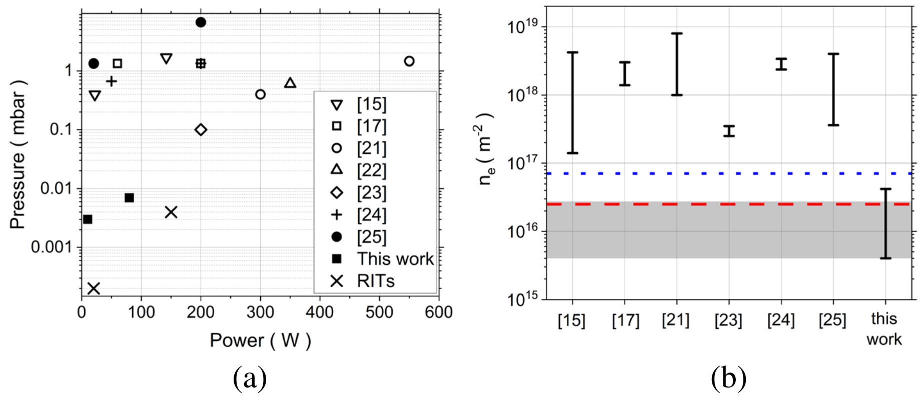

Fig. 1 **a** Comparison of the pressure and power ranges of ICPs experimentally studied using THz-TDS in the literature and in this work. Crosses indicate typical operating conditions for RITs [27]. The pressure range of RIT operation is significantly lower than what has been investigated in prior THz-TDS research, yet it aligns with the conditions explored in this study. **b** This is also reflected in the electron densities prevalent in the respective plasmas. The line integrated densities reported in previous studies are shown, together with the line integrated densities obtained in this work. For comparison, values for a RIT-10 are indicated by the gray area [13]. Typical line integrated densities for Hall thrusters and Kaufmann ion engines are also shown by the red dashed line and the blue dotted line, respectively [28, 29]

for the application of THz-TDS. As illustrated, our work is the first to reach values corresponding to typical ion thruster operating conditions.

We focus on the investigation of xenon plasmas and strengthen our results by also including argon and krypton for validation. While previous studies have predominantly examined argon plasmas, xenon offers distinct advantages, such as achieving a higher degree of ionisation at lower input power. Moreover, xenon is currently one of the primary propellants utilized in commercially deployed GIEs, making it highly relevant from an applied perspective.

Experimental setup

To validate the capability of THz-TDS for characterizing plasmas within GIEs, an ICP mirroring plasma conditions used in operational RITs is simulated. The corresponding experimental setup is shown schematically in Fig. 2.

A plasma is ignited inside a quartz glass cylinder (20 cm length, 6.9 cm outer diameter and 3 mm thickness) by applying a pressure shock or voltage spark. The energy to maintain the plasma is coupled into the discharge chamber by a coil with 8 windings connected to a radio frequency generator (RFG), thus generating an inductively coupled plasma. For xenon, the supply power of the RFG P_{RFG} is varied between 10 W and 60 W to maintain a stable discharge. If the coupling power is less then $\approx$ 8 W, the coupling energy is not sufficient to sustain the plasma. The excitation frequency is about 2.4 MHz for all measurements.

The gas inlet is perpendicular to the glass cylinder and the propellant flow is controlled by a mass flow controller (MFC) with an output between 0.5 - 50 sccm. The mass flow is not limited to the quartz cylinder. For further analysis, the assumption is made that for every measurement point a steady-state of propellant flow is reached inside the chamber. This is verified by a simplified free molecular flow (fmf) model of the setup in the

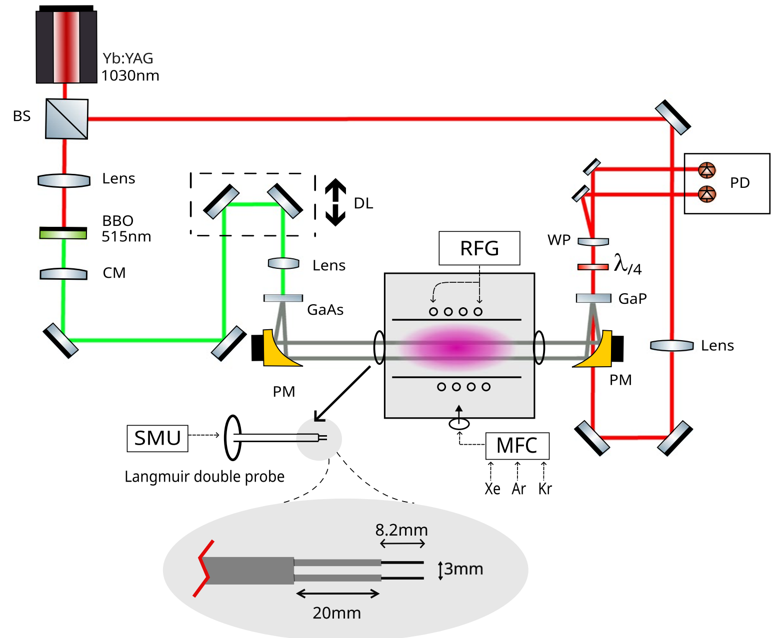

Fig. 2 Experimental setup for measuring the properties of ICPs using THz-TDS and a Langmuir double probe. The schematic depicts the main components within and around the vacuum chamber, represented by the greyed square between the parabolic mirrors. Inside the chamber, a glass cylinder, supported by two aluminum brackets and wrapped with an insulated coil to prevent short circuits, is shown. The left flange of the chamber can be alternated between one equipped with a THz-window and one designed to hold the Langmuir double probe and its electrical connections. The geometries of the Langmuir probe are outlined schematically with the ceramic tube in dark gray and the electrodes in black. Key components of the setup include: BS (beamsplitter), BBO (barium borate nonlinear optical crystal), CM (collimator), DL (delay line), PM (parabolic mirror), SMU (source measure unit), RFG (radio frequency generator), MFC (mass flow controller), WP (Wollaston prism), and PD (photodiodes)

multi physics simulation software COMSOL. The absolute pressure in the chamber is measured with a capacitive transmitter (Leybold CERAVAC CTR 101 N), allowing pressure measurements independent of the type of gas used. In our setup, a high vacuum is achieved by pumping with a roughing pump and a turbomolecular pump. Due to the size of the chamber, a cube of 25 cm edge length, the turbomolecular pump was adapted by installing a copper membrane reducing the inlet diameter from 10 cm to 1.5 cm. Thus, we are able to generate a background pressure in the order of 10^{-4} mbar. Plasma discharge is obtained at a chamber pressure of 10^{-3} to 10^{-2} mbar.

Windows are installed on both sides of the chamber, aligned along the radial center of the plasma discharge. These windows offer high transparency for THz radiation at frequencies below 1.7 THz.

Diagnostics and modeling

THz-TDS

We employ an Yb:YAG oscillator operating at 78 MHz repetition rate with a central wavelength of 1030 nm and a pulse length of 100 fs. A beamsplitter reflects roughly 3% of the oscillator's 8.7 W output power as a gating pulse for electro-optical sampling, while the transmitted portion is focused onto a BBO crystal to generate

300 mW at a central wavelength of 515 nm by second harmonic generation. A short-pass filter removes the 1030 nm residual, and the second harmonic of the laser is directed to a delay stage before being focused onto a THz antenna. The THz antenna is modulated with a 4 kHz square wave voltage of 10 V resulting in modulated single-cycle THz pulses. The THz pulses are collimated by a parabolic mirror and transmitted through the ICP chamber before being focused by a second parabolic mirror onto a 2 mm thick GaP crystal. At this point, the THz radiation overlaps spatially with the gate pulse, which is focused onto the GaP crystal by a lens for electro-optical sampling of the THz pulse. The linear polarized gate pulse is then circularly polarized by a quarter waveplate before being separated by a Wollaston prism into two orthogonal polarized beams. These linearly polarized beams are detected by two photodiodes the response time of which is optimized for this modulation frequency. A lock-in detection scheme reads out the intensity difference between them at the 4 kHz modulation frequency. The experimental setup is schematically shown in Fig. 2. By tuning the delay stage, the entire THz pulse is electro-optically sampled in the time domain by the optical gate pulse. Fourier transformation converts the time domain data into the frequency domain where the complex dielectric function of the plasma under study can be calculated in the detection range from 100 GHz to 1.7 THz. We compare a reference measurement through the ICP without plasma $E_{\mathrm{Ref}}(\omega)$ with a measurement with plasma $E_{\mathrm{p}}(\omega)$. The magnitude ratio of $E_{\mathrm{p}}(\omega)$ and $E_{\mathrm{Ref}}(\omega)$ is denoted by $T(\omega)$, while $\phi(\omega)$ is the phase difference. The real part of the refractive index $n(\omega)$ and the absorption coefficient $\alpha(\omega)$ can be found using the following equations [19]

$$n(\omega) = 1 + \frac{\phi(\omega)c}{\omega d} \tag{2}$$

and

$$\alpha(\omega) = -\frac{2}{d}\ln(T(\omega)), \tag{3}$$

where d is the length of the plasma inside the discharge chamber and c is the speed of light in vacuum. Note that we assume for the calculation of the absorption that there is no reflection at the interface due to the gradual transition into the plasma. However, since the absorption is negligible in the density range investigated here, it ultimately makes no difference whether a reflection at the smooth interface is taken into account or not. Hence, the real and the imaginary parts of the dielectric function of the ICP are determined by the following equations [30]

$$\Re(\varepsilon(\omega)) = \varepsilon^{'}(\omega) = n(\omega)^2 - \left(\frac{c\alpha(\omega)}{2\omega}\right)^2, \tag{4}$$

$$\Im(\varepsilon(\omega)) = \varepsilon^{''}(\omega) = \frac{cn(\omega)\alpha(\omega)}{\omega}. \tag{5}$$

To extract valuable information from the complex dielectric function, we fit a Drude model to the data. The model is given by:

$$\Delta\varepsilon(\omega) = -\frac{e^2}{d\epsilon_0 m}\frac{n_e}{\omega^2 + i\omega\Gamma}, \tag{6}$$

where $\Delta\epsilon(\omega)$ is the plasma induced dielectric function change, ϵ_0 represents the vacuum permittivity, and m and e denote the electron mass and elementary charge, respectively. By fitting this model to the data, we can determine the electron density n_e and the carrier damping rate Γ [31, 32], which in plasma physics is also referred to as the electron collision frequency ν. Since we do not take into account a possible intensity profile of the plasma, we obtain the line averaged value of the electron density of the plasma.

Global model

We employ a global plasma model for comparing the averaged electron densities measured by THz-TDS in the plasma of our experimental setup with theoretical values. The global plasma model is based on a publication by Chabert et al. [3]. This model consists of four differential equations which determine the time evolution of neutral gas and electron temperature, neutral gas density, and ion (or electron) density. By solving these differential equations, we can derive the densities and temperatures in dynamic equilibrium. However, since the plasma model was originally developed for radio-frequency ion thrusters, we have to make some modifications to adapt the model to our setup. These adjustments concern primarily the geometric parameters of the model. Contrary to RITs, our setup lacks a grid system. Furthermore, there is a neutral gas pressure present in the entire chamber and the plasma discharge takes place in a volume smaller than that of the vacuum chamber. We determine the neutral gas pressure with a pressure gauge and evaluate the spatial extent of the plasma with photogrammetric methods. The precise alterations of the model are presented directly based on the differential equations to be solved. According to the model of Chabert et al., the temporal change of the ion and electron density n_e, which are equal in a quasineutral plasma neglecting the higher charged ions, is determined by balancing the source and loss terms

$$\frac{\mathrm{d}n_\mathrm{e}}{\mathrm{d}t} = n_\mathrm{e} n_\mathrm{g} K_\mathrm{iz} - n_\mathrm{e} u_\mathrm{B}\frac{A_\mathrm{eff}}{V}\,. \tag{7}$$

Here, t is the time, n_g the neutral gas density at the location of the plasma discharge, K_iz the rate coefficient of ionisation, u_B the Bohm velocity, and V the volume of the plasma discharge. All rate coefficients K_i used with given specific cross-sections are calculated assuming a Maxwellian electron energy distribution function

$$K_i(T_\mathrm{e}) = \int_0^\infty \sigma_i(E)\sqrt{\frac{2E}{m}} f_{T_\mathrm{e}}(E)\mathrm{dE} \tag{8}$$

with

$$f_{T_\mathrm{e}}(E) = 2\sqrt{\frac{E}{\pi}}(k_\mathrm{B}T_\mathrm{e})^{-\frac{3}{2}}\exp\left(-\frac{E}{k_\mathrm{B}T_\mathrm{e}}\right). \tag{9}$$

For all processes involving argon and xenon, as well as the excitation processes for krypton, the underlying cross-sections were taken from the Biagi database [33]. These data sets are based on the Fortran code MagBoltz version 8.9 and higher. For elastic collisions, data from the Complex Optical Potential database was used for all three gases [34]. The remaining processes of krypton were taken from an older version of the Biagi database [35]. In the case of our experimental setup, it is necessary to adapt the loss term. It describes the loss of ions leaving the plasma at the Bohm velocity. The corresponding effective loss area is given by

$$A_{\text{eff}} = 2h_R \pi R L_{\text{Plasma}} + 2h_L \pi R^2 \,. \tag{10}$$

L_{Plasma} is the length of the plasma discharge and R is the radius of the glass cylinder where the discharge takes place (see Fig. 2). h_R and h_L are factors that relate the plasma density at the centre of the discharge to the plasma density at the front surface and at the lateral surface of the glass cylinder, respectively. The source term in Eq. 7 is unchanged compared to the publication by Chabert et al. and describes the production of ions by impact ionisation. The temporal change of the neutral gas density is also determined by Chabert et al. by balancing the source and loss terms. In our model, the equation takes the form

$$\frac{\mathrm{d}n_{\mathrm{g}}}{\mathrm{d}t} = n_{\mathrm{e}} u_{\mathrm{B}} \frac{A_{\text{eff1}}}{V} - n_{\mathrm{e}} n_{\mathrm{g}} K_{\text{iz}} + \frac{1}{4} v_{\mathrm{g}} \left(n_{\mathrm{g0}} - n_{\mathrm{g}} \right) \frac{2\pi R^2}{V} \,. \tag{11}$$

The first term describes the generation of neutral gas particles by ions recombining on the surface of the glass cylinder. The effective area for this process is accordingly given by

$$A_{\text{eff1}} = 2h_R \pi R L_{\text{Plasma}} \,. \tag{12}$$

The second term is the same as that used by Chabert and describes losses by ionisation. The last term balances the neutral gas flow into and out of the discharge area through the open faces of the glass cylinder. v_{g} is the mean thermal velocity of the neutral gas particles. n_{g0} is the neutral gas density inside the vacuum chamber surrounding the glass cylinder. Assuming an ideal gas, n_{g0} can be derived by experiment with the neutral gas pressure measured via the pressure gauge connected to the vacuum chamber. In the case of the temporal change of the electron temperature, the effective loss area for ions must be adjusted in the same way as for the temporal change of the ion density compared to the original publication by Chabert et al.. The change in the electron temperature over time is determined by analysing the average thermal energy of the electrons. For this purpose, the absorbed power density and the power loss density are balanced as shown in Eq. 13

$$\frac{\mathrm{d}}{\mathrm{d}t} \left(\frac{3}{2} n_{\mathrm{e}} k_{\mathrm{B}} T_{\mathrm{e}} \right) = p_{\text{abs}} - p_{\text{loss}} \,. \tag{13}$$

The absorbed power density is calculated directly via the coil current and the real part of the complex impedance of the coil with the plasma in it

$$p_{\text{abs}} = \frac{1}{2V} R_{\text{ind}} I_{\text{coil}}^2 \,. \tag{14}$$

The calculation of R_{ind} and I_{coil} can be taken from the original publication by Chabert et al., the power loss density as well, but needs to be slightly modified

$$p_{\text{loss}} = E_{\text{iz}} n_{\text{e}} n_{\text{g}} K_{\text{iz}} + E_{\text{exc}} n_{\text{e}} n_{\text{g}} K_{\text{exc}} + 3\frac{m}{M} k_{\text{B}} \left(T_{\text{e}} - T_{\text{g}}\right) n_{\text{e}} n_{\text{g}} K_{\text{el}} + 7 k_{\text{B}} T_{\text{e}} n_{\text{e}} u_{\text{B}} \frac{A_{\text{eff}}}{V} . \tag{15}$$

It is made up of four terms. The first two terms describe the power loss due to ionisation and excitation. E_{iz} stands for the ionisation energy and E_{exc} for the average excitation energy of the respective gas atom. It should be noted that the average excitation energy itself is also a function of the electron temperature and is determined by averaging the rate coefficients of the individual excitation processes. K_{exc} is the sum of all rate coefficients of the individual excitation processes. The third term describes the energy transfer from the electrons to the neutral gas with the temperature T_{g} and the atomic mass M by elastic collisions. The elastic collisions are taken into account here by the rate coefficient K_{el}. The last term describes the energy transfer of the electrons to the wall of the glass cylinder. In contrast to the original publication by Chabert et al., the effective area A_{eff} is used here. The sum of the power absorbed by the plasma and the power dissipated in the coil due to ohmic losses gives the power provided by the RF generator within the framework of the model

$$P_{\text{RFG}} = P_{\text{abs}} + P_{\text{ohm}} = \frac{1}{2}(R_{\text{ind}} + R_{\text{ohm}}) I_{\text{coil}}^2 . \tag{16}$$

P_{RFG} is the power provided by the RF generator, P_{abs} the power absorbed by the plasma, P_{ohm} the power dissipated by ohmic losses in the coil and R_{ohm} the ohmic resistance of the coil. It should be noted that the temporal evolution of the neutral gas temperature is not taken into account in contrast to the original publication and a constant neutral gas temperature is assumed. Calculations with different neutral gas temperatures show that the other plasma parameters change negligibly over a wide range of neutral gas temperatures. The reason for this is the weak coupling between neutral gas and electron temperature due to the large mass difference between neutral gas atoms and electrons. For the sake of accuracy, a minimum and maximum value for the temperature T_{g} is approximated. The temperature is noticeably higher than standard room temperature, but lower than 400 K, since hotter conditions would have melted insulating tape inside the chamber. The gas temperature can therefore be approximated to be in the range between 320 K and 400 K. All electron densities derived by the global model are therefore displayed in the graphs as a small interval corresponding to the possible temperature range. The degree of ionisation can be calculated by dividing the electron densities by the total gas densities. The total gas density n_t can be estimated using the ideal gas law

$$n_{\text{t}} = \frac{P_{\text{ch}}}{k_{\text{B}} T_{\text{g}}} \tag{17}$$

where P_{ch} is the chamber pressure. While the impact of the temperature uncertainty is very small on the values of the electron densities obtained with the global model, it is slightly more significant when it comes to the ideal gas law. However, this rough estimate is enough to highlight the qualitative behaviour of the degree of ionisation and to provide its approximate magnitude. Figure 3 shows the calculated degree of ionisation α, predicted with the global model. The degree of ionisation α is highest for xenon and ranges from $7 \cdot 10^{-4}$ to $4 \cdot 10^{-3}$ for powers between 10 W and 60 W.

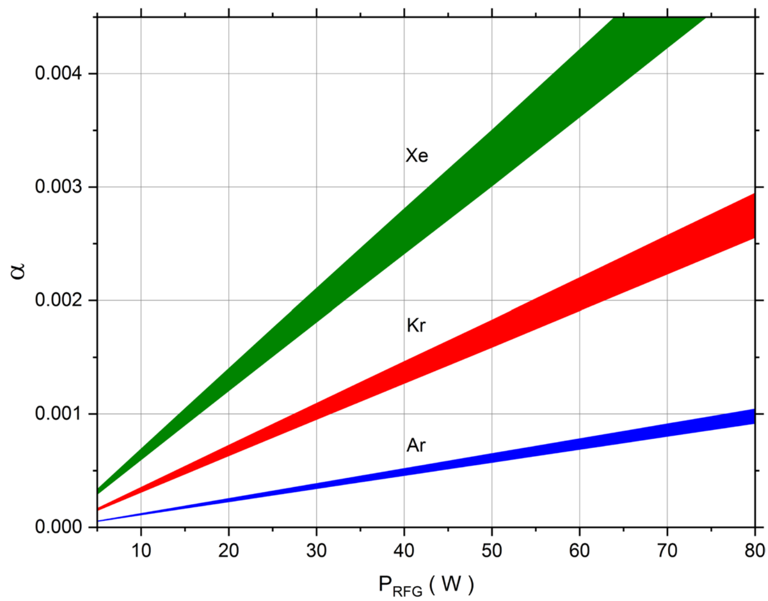

Fig. 3 Comparison of the approximate degree of ionisation α for xenon ($P_{ch} \approx 3 \cdot 10^{-3}$ mbar), krypton ($P_{ch} \approx 3.6 \cdot 10^{-3}$ mbar) and argon ($P_{ch} \approx 7 \cdot 10^{-3}$ mbar). For simplicity only the averaged electron densities obtained with the global model were used. The highest degree of ionisation is achieved with the lower gas temperature, 320 *K*, while the lower edge of each couloured area represents 400 K

To facilitate the comparison of model results with experimental data, it is essential to consider the operational principles of THz-TDS and Langmuir double probe measurements. The Langmuir double probe measurement provides a means to assess the electron density at a single point within the plasma. Conversely, THz-TDS offers an averaging measurement of the electron density along the entire path of the THz beam in the plasma chamber, assuming a uniform distribution of the plasma. Since the Langmuir double probe was positioned in the centre of the plasma discharge, the model results of the electron density n_e can be simply adapted by scaling up to the centre electron density. For comparison with the THz-TDS, a plasma profile $H(r,z)$ of the form

$$H(r,z) = \sqrt{\left(1 - \left(\sqrt{1-h_R^2}\frac{r}{R}\right)^2\right)\left(1 - \left(\sqrt{1-h_L^2}\frac{2z}{L_{\text{Plasma}}}\right)^2\right)} \tag{18}$$

is assumed where r and z are the radial and axial position, respectively, within the plasma discharge. The plasma profile given is a heuristic function proposed in Ref. [36]. For $r = 0$, the function is integrated from $-0.5L_{\text{Plasma}}$ to $0.5L_{\text{Plasma}}$ and the result is multiplied by the electron density to calculate the mean density along the line of sight of the THz beam.

Langmuir double probe

The validity of the electron densities measured by THz-TDS is further verified experimentally using a Langmuir double probe. Langmuir probes are often favored for plasma diagnostics due to their relative simplicity and cost-effectiveness. In this study, a double probe configuration is employed, as it offers more reliable performance in an RF environment compared to single probes and no reference electrode in the plasma is needed. Although in the ideal case a double probe would not experience any RF-pickup, it should be mentioned that this may not be guaranteed in reality and the lack of an RF-compensation may be a possible source of uncertainty. However, research under similar conditions were successfully carried out without an RF-compensation [15]. The two tungsten tips combined measure an area of $1.5 \cdot 10^{-5}$ m^2 with a diameter of 0.3 mm for each tip. A thin ceramic tube around each electrode is added to prevent short circuits arising from material deposited due to sputtering [10]. Figure 2 depicts the schematics of the probe and its integration into the experimental setup, with the probe tips oriented parallel to the magnetic field of the RF coil. Figure 4a presents a series of IV-curves acquired for xenon using the Langmuir double probe, illustrating their evolution with varying RFG supply power, i.e. power coupled into the plasma. To obtain these curves, we performed current measurements at the probe by sweeping the applied DC voltage using a precision source/measure unit (Keysight B2901A). The voltage was systematically varied in the range from −40 V to +40 V in 10 mV increments. Each step lasted for 2 ms. At each setting, we conducted two measurements, and subsequently, the resulting electron densities were averaged. The deviations between the individual measurements were found to be small (< 1%). This of course only represents the statistical reproducibility and can only serve as a first-order estimate of the uncertainty.

One limitation of Langmuir double probes is their inability to directly access the EEDF. Therefore, when analyzing the acquired IV-characteristics, an assumption of a Maxwell-Boltzmann distribution for the electrons is required. In our analysis, we followed the approach outlined in Refs. [12] and [13], since it is more robust against deviations from the ideal theory than the standard procedure. There a polynomial fit is used to obtain the

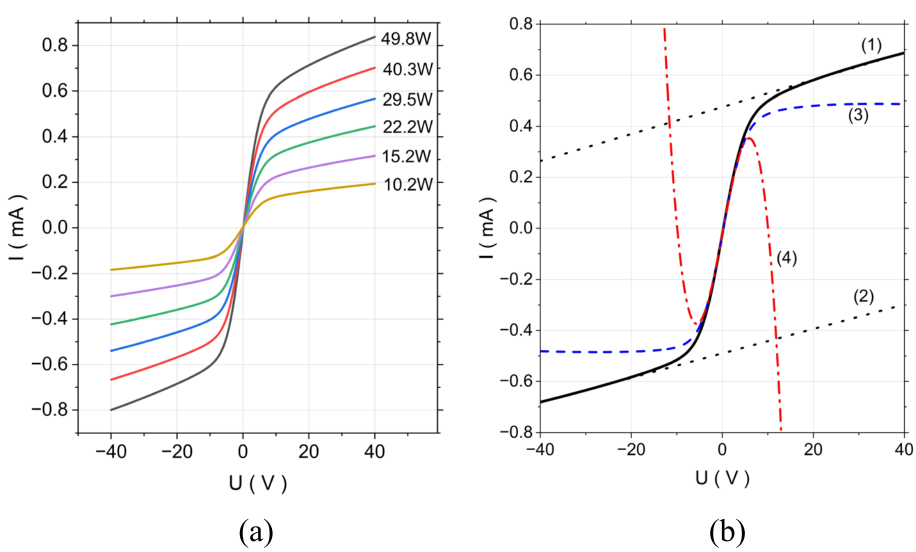

Fig. 4 **a** Development of IV-characteristics of the double probe for xenon at a chamber pressure of ≈ $3 \cdot 10^{-3}$ mbar for varying RFG powers. **b** The evaluation process of a Langmuir double probe measurement exemplary shown for a xenon measurement at a RFG power of 40W and a chamber pressure of ≈ $3 \cdot 10^{-3}$ mbar. The linear sheath fits (2) are substracted from the measured IV-characteristic (1) to obtain the corrected characteristic curve (3). After determining the ion saturation current with the corrected curve, a polynomial fit (4) provides the maximum slope that corresponds to the electron temperature

maximum slope of the corrected and normalized curve. Using this information, we calculate both the electron temperature and, subsequently, the electron density. An example of this analysis is illustrated in Fig. 4b.

As shown in Fig. 5, the results of the Langmuir double probe measurements agree well with those of the theoretical model described above. The measured electron densities have similar absolute values than those derived by the global model and they increase approximately linear with the coupling power as expected for low temperature plasmas with a low degree of ionisation [37]. Note that, in contrast to THz-TDS, both methods assume a Maxwellian distribution for the electrons. Since the Langmuir double probe measures in the center of the plasma volume, the obtained electron densities have to be compared with the maximum values of the global plasma model and not with the averaged values along the THz beam direction. This corresponds to $r = 0$ and $z = 0$ in Eq. 18.

Results and discussion

THz-TDS

Figure 6 presents two THz pulses in the time-domain: one transmitted through a neutral gas atmosphere inside the discharge chamber and the other through an ignited xenon plasma. The plasma is generated at a chamber pressure of $\approx 3 \cdot 10^{-3}$ mbar with an RFG power of ≈ 47 W. The reference measurements are taken under identical conditions but without plasma ignition. The blue dotted curve in Fig. 6 highlights the difference between the THz pulses transmitted through the plasma (Plasma) and through the neutral gas (Reference), demonstrating that the difference between the two pulses

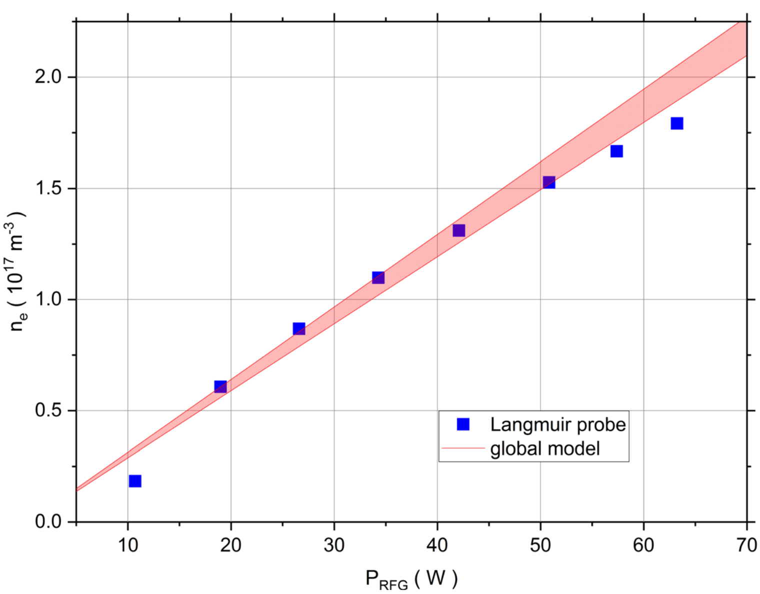

Fig. 5 Exemplary comparison of the Langmuir double probe measurements and the maximum electron densities obtained by the global model for krypton at a chamber pressure of $\approx 3.6 \cdot 10^{-3}$ mbar and varying RFG power. Note that unlike Fig. 8 this figure does not show the length averaged densities of the model because the Langmuir probe performs a bulk measurement at maximum density. The density calculated with the global plasma model is represented by an area instead of a single line to account for the uncertainty in neutral gas temperature. For a detailed discussion see "Global model" section

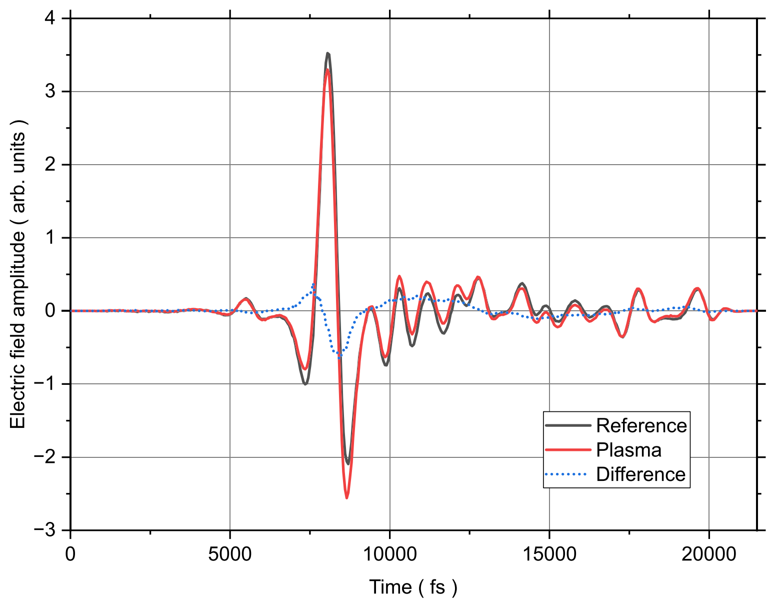

Fig. 6 THz pulses in time-domain for a chamber pressure of $\approx 3 \cdot 10^{-3}$ mbar and a RFG power of $P_{\mathrm{RFG}} \approx$ 47 W with plasma ignition (red) and its reference without plasma ignition (black). The blue dotted curve represents the difference between both pulses.

is clearly measurable. Here, high pulse repeatability and high temporal resolution are crucial to measure the lowest electron densities reported in this paper. Our analysis of pulse repeatability indicates that the frequency-dependent phase of the reference pulses is reproducible with deviations of less than 0.3% between 0.1 THz and 0.2 THz and less than 0.05% between 0.2 THz and 1 THz.

Ignition was achieved by either a pressure shock or the application of a high-voltage spark, and measurements began as soon as the chamber reached a steady-state. Maintaining the chamber pressure by a constant mass flow rate whilst increasing the RFG power allowed observation of the ICP evolution. With increasing power, both the degree of ionisation and the electron density increase, which leads to a corresponding increase in the plasma frequency ω_p of the discharge. In Fig. 7a the evolution of $\Delta\Re(\varepsilon(\omega))$ is shown for three operating points at $\approx 3 \cdot 10^{-3}$ mbar chamber pressure.

In Fig. 7b, $\Delta\Re(\varepsilon(\omega))$ is exemplary fitted by the Drude model. This fitting allows us to extract the electron density n_e for a xenon plasma at 35.2 W and a chamber pressure of $\approx 3 \cdot 10^{-3}$ mbar. By systematically varying the power being coupled into the plasma and applying the same fitting procedure, we track the evolution of n_e as a function of input power. The electron densities obtained for xenon, krypton, and argon are illustrated in Fig. 8. Across all three gases, an almost linear increase in electron density with increasing RFG power is observed, consistent with both THz-TDS and Langmuir probe measurements. Our THz-TDS setup achieves high sensitivity, enabling us to measure electron densities as low as $\approx 2 \cdot 10^{16}$ m^{-3} for each gas. This represents a significant extension of the technique to lower electron densities compared to previous studies and effectively probes the density ranges typical in GIEs. Specifically, for xenon, the electron density increases from $\approx 2 \cdot 10^{16}$ m^{-3} at 10 W RFG power to $\approx 2.1 \cdot 10^{17}$ m^{-3} at 57 W RFG power, demonstrating the steepest rise among the gases. In contrast, argon

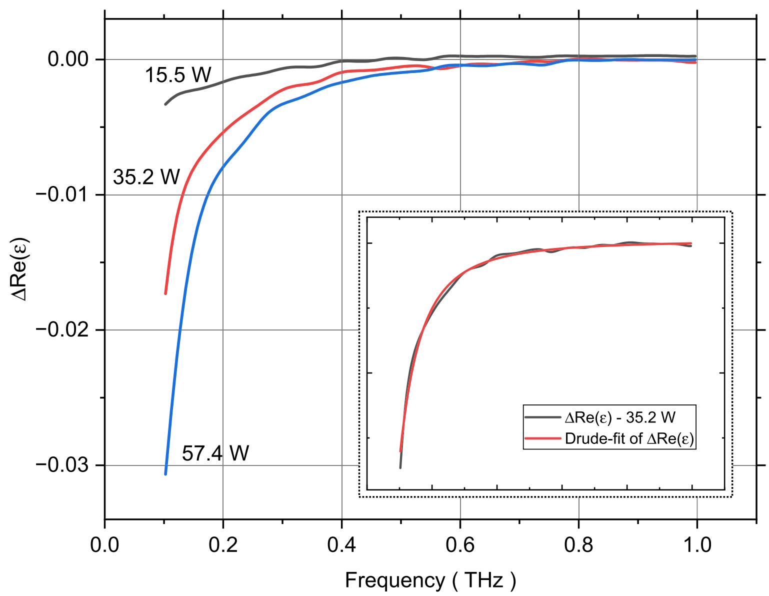

Fig. 7 **a** Change of the real part of the dielectric function of a Xe plasma at 15.5 W, 35.2 W and 57.4 W at $\approx 3 \cdot 10^{-3}$ mbar chamber pressure as function of frequency in THz. **inset** Drude-fit to the change of the real part of the dielectric function at 35.2 W

shows a more gradual increase, with electron densities rising from $\approx 4 \cdot 10^{16}$ m^{-3} at 28 W RFG power to $\approx 1.4 \cdot 10^{17}$ m^{-3} at 72 W RFG power. Krypton falls between xenon and argon, with electron densities increasing from $\approx 2 \cdot 10^{16}$ m^{-3} at 10 W RFG power to $\approx 1 \cdot 10^{17}$ m^{-3} at 57 W.

The considerably lower electron density observed for argon, compared to xenon and krypton, is due to argon's higher ionisation energy, which is 12.6% and 29.9% greater than that of krypton and xenon, respectively. This higher ionisation energy results in a lower plasma frequency ω_p, which can fall outside the accessible THz range. To address this and ensure argon's plasma frequency remained detectable, the mass flow-and consequently the chamber pressure-was increased to $\approx 7 \cdot 10^{-3}$ mbar, enabling a meaningful comparison across all three gases.

Our results are consistent with classical plasma physics predictions [38], demonstrating that THz-TDS is highly effective for characterizing low-pressure ICPs, such as those found in GIEs and other electric propulsion systems. Furthermore, our findings closely correlate with those of Esteves et al., who reported similar electron density values for various noble gases in radio-frequency ICPs using Langmuir probes [39]. The trends observed in their study are remarkably consistent with our THz-TDS results, underscoring the robustness and reliability of this non-invasive diagnostic method.

Comparison of THz-TDS measurements with Langmuir measurements and theoretical modeling

Good agreement is observed when comparing the electron densities obtained by the two experimental methods (THz-TDS and Langmuir probe) and the global modeling approach. While the Langmuir probe yields peak electron density values, the THz-TDS

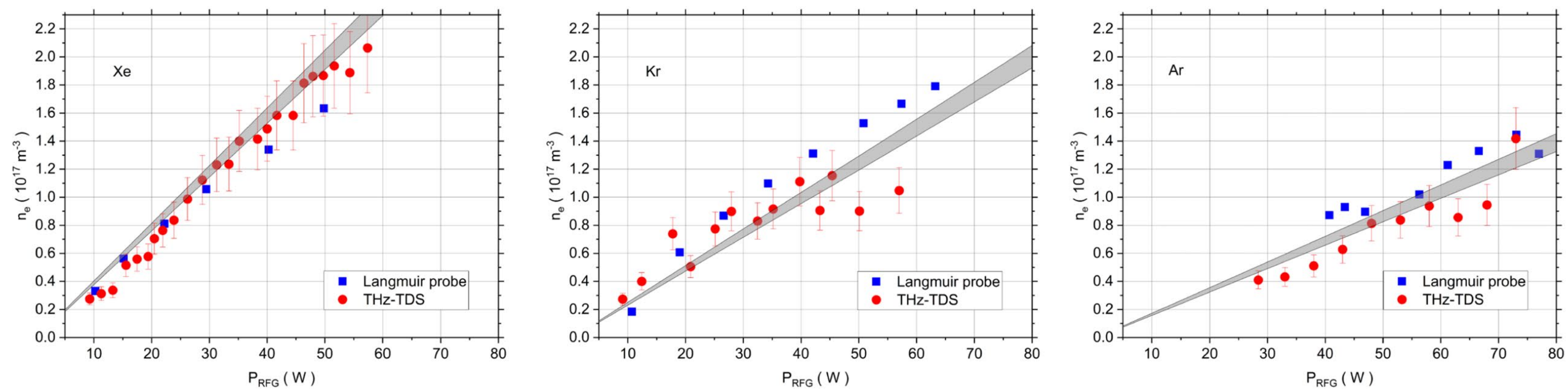

(a) Xenon (b) Krypton (c) Argon

Fig. 8 Comparison of electron densities obtained using THz-TDS (red dots), the Langmuir double probe (blue squares), and the theoretical model (grey area) for all three noble gases. The Langmuir probe measurements have been converted to average electron densities based on the assumed spatial plasma distribution (see Eq. 18). The grey area represents the theoretically predicted average densities, covering the estimated temperature range. The chamber pressure was set to $\approx 3 \cdot 10^{-3}$ mbar for xenon and to $\approx 3.6 \cdot 10^{-3}$ mbar for krypton. To ensure reliable results for argon, the chamber pressure was increased to $\approx 7 \cdot 10^{-3}$ mbar, and higher coupling power was required to maintain a stable plasma, particularly when the Langmuir probe was introduced. The experimentally determined electron densities agree well with the expected behavior based on the calculated degrees of ionisation shown in Fig. 3. The error bars represent the statistical reproducibility of the obtained values in the middle of the shown range. The value is then extrapolated percentually for all given values measurements provide average values under the uniformity approximation, as discussed above. To enable direct comparison between the methods, the peak electron densities from the Langmuir probe measurements are converted into average values using the assumed spatial distribution given in Eq. 18. Figure 8a illustrates the electron densities for xenon, where the best match between experimental results and the theoretical model is achieved. This strong agreement is attributed to the higher degree of ionisation in xenon plasmas, leading to elevated electron densities that shift the plasma frequency further into the THz range, resulting in more significant phase shifts that are readily detected by THz-TDS.

The electron densities obtained for krypton are presented in Fig. 8b. Although the THz-TDS data exhibit greater variance than the Langmuir probe data, our analysis indicates that the measurements remain broadly consistent with a linear increase in electron density, within the representative error bars, as the RFG power is raised. The lower degree of ionisation in krypton, combined with the limited dataset, makes it more challenging to discern a clear trend amidst statistical fluctuations. Notably, the two data points measured at the two highest RFG power levels appear suspiciously like statistical outliers, which give the impression of a non-linear increase of electron density with RFG power. However, when viewed in their entirety, the krypton measurements remain broadly consistent with the expected behaviour of increasing electron density with increasing RFG power, in line with the results observed for xenon and in agreement with the Langmuir probe measurements. When comparing the densities of xenon and krypton, it is evident that krypton produces a lower electron density at the same coupling power and similar neutral gas density. A similar trend is observed in the argon measurements, as depicted in Fig. 8c. However, conducting measurements with argon introduces additional challenges due to its inherently less stable discharge. Maintaining a stable argon plasma becomes particularly challenging in the presence of the Langmuir double probe, preventing stable operation at low coupling powers. As a result, measurements below 40 W were only feasible using THz-TDS. This highlights the benefits of a non-invasive technique such as THz spectroscopy established here.

Conclusion

This study explores the application of THz-TDS as a non-invasive tool for plasma characterization, specifically targeting low-pressure inductively coupled plasmas typically found in the nominal operating modes of gridded ion thrusters. Our findings confirm the effectiveness of THz-TDS in these conditions, showing strong correlations and good agreement with both theoretical models and the well-established yet invasive Langmuir probe method. Notably, THz-TDS is adaptable across a broad pressure range, as it can be fine-tuned for lower electron densities by extending the frequency range further into the GHz domain.

Our results underscore the potential of THz-TDS for future investigations into low-pressure plasmas, proving it to be a valuable tool for analyzing plasmas akin to those in operational gridded ion engines. The next step towards fully integrating this method into the characterization of plasmas in flight-qualified engines involves applying THz-TDS to ICPs during ion extraction, further solidifying its role in advanced plasma diagnostics.

Nomenclature

EEDF electron energy distribution function
GaAs gallium arsenide
GIE gridded ion engine
ICP inductively coupled plasma
MFC mass flow controller
PCA photoconductive antenna
RF radio frequency
RFG radio frequency generator
RIT radio frequency ion thruster
SMU source measure unit
TDS time-domain spectroscopy
THz terahertz

Authors' contributions

K.B. and R.S.R. assembled the plasma discharge chamber, carried out all the measurements, evaluated the data and created the first draft of the manuscript. M.S. set up the optical components for the THz-TDS and supervised measurements and data analysis. K.K. adapted the theoretical model to the experimental setup, derived data using this model and wrote the corresponding part of the manuscript. K.H. had the idea for the experiment and supervised the laboratory work. F.B., J.Z. and K.K. always provided support in case of technical problems with the experiment. K.W. helped in setting up the discharge chamber. P.J.K. and S.C. supervised the work. All authors contributed to the study conception and design and commented on previous versions of the manuscript, read and approved the final manuscript.

Funding

Open Access funding enabled and organized by Projekt DEAL. We acknowledge support through the European Regional Development Fund (ERDF) for the project "Innovationslabor Prozessdiagnostik" under contract 21031934. SC thanks the State of Hesse Landes-Offensive zur Entwicklung Wissenschaftlich-ökonomischer Exzellenz (LOEWE) for awarding him the Transfer-Professur „Hochtechnologiematerialien".

Data availability

Data sets obtained during the current study are available from the corresponding author upon reasonable request.

Code availability

Not applicable.

Declarations

Competing interests

The authors declare no competing interests.

Received: 15 September 2024 Accepted: 25 January 2025
Published online: 25 February 2025

References

1. Mazouffre S (2016) Electric propulsion for satellites and spacecraft: established technologies and novel approaches. Plasma Sources Sci Technol 25(3):033002
2. Holste K, Dietz P, Scharmann S, Keil K, Henning T, Zschätzsch D, Reitemeyer M, Nauschütt B, Kiefer F, Kunze F, Zorn J, Heiliger C, Joshi N, Probst U, Thüringer R, Volkmar C, Packan D, Peterschmitt S, Brinkmann KT, Zaunick HG, Thoma MH, Kretschmer M, Leiter HJ, Schippers S, Hannemann K, Klar PJ (2020) Ion thrusters for electric propulsion: Scientific issues developing a niche technology into a game changer. Rev Sci Instrum 91(6):061101
3. Chabert P, Arancibia Monreal J, Bredin J, Popelier L, Aanesland A (2012) Global model of a gridded-ion thruster powered by a radiofrequency inductive coil. Phys Plasmas 19(7):073512
4. Dale E, Jorns B, Gallimore A (2020) Future directions for electric propulsion research. Aerospace 7:9
5. Hieftje GM (1992) Plasma diagnostic techniques for understanding and control. Spectrochim Acta B Atomic Spectrosc 47(1):3–25
6. Goebel DM, Katz I (2008) Fundamentals of Electric Propulsion. John Wiley I & Sons, Ltd. ISBN 9780470436448
7. Kersten H (2023) Diagnostics for electric propulsion systems. EPJ Tech Instrum 10(1):12
8. Shul RJ, Pearton SJ (2000) Handbook of Advanced Plasma Processing Techniques. Springer, Berlin, Heidelberg. ISBN 978-3-540-66772-8
9. Gottscho RA, Miller TA (1984) Optical techniques in plasma diagnostics. Pure Appl Chem 56(2):189–208

10. Lobbia RB, Beal BE (2017) Recommended practice for use of langmuir probes in electric propulsion testing. J Propuls Power 33(3):566–581
11. Godyak V (2021) RF discharge diagnostics: Some problems and their resolution. J Appl Phys 129(4):041101
12. Nauschütt BT, Chen L, Holste K, Klar PJ (2021) Non-invasive assessment of plasma parameters inside an ion thruster combining optical emission spectroscopy and principal component analysis. EPJ Tech Instrum 8(1):13
13. Nauschütt BT (2022) Combining optical emission spectroscopy and multivariate data analysis methods for an empirical assessment of plasma parameters of ion thrusters. PhD thesis, Justus-Liebig-Universität Gießen
14. Jamison SP, Shen J, Jones DR, Issac RC, Ersfeld B, Clark D, Jaroszynski DA (2003) Plasma characterization with terahertz time–domain measurements. J Appl Phys 93(7):4334–4336
15. Ando A, Kurose T, Reymond V, Kitano K, Kitahara H, Takano K, Tani M, Hangyo M, Hamaguchi S (2011) Electron density measurement of inductively coupled plasmas by terahertz time-domain spectroscopy (THz-TDS). J Appl Phys 110(7):073303
16. Meier SM, Tsankov TV, Luggenhölscher D, Czarnetzki D (2017) Measurement of plasma densities by dual frequency multichannel boxcar THz time domain spectroscopy. J Phys D Appl Phys 50:245202–245215
17. Brown NP, Steinberg AM, Deibel JA, Walker ML (2020) Assessment of the Capability of Terahertz Time-Domain Spectroscopy as a Plasma Diagnostic. In: Proceedings of the AIAA Propulsion and Energy 2020 Forum, Virtual Event. American Institute of Aeronautics and Astronautics. https://doi.org/10.2514/6.2020-3647
18. Kolner BH, Buckles RA, Conklin PM, Scott RP (2008) Plasma characterization with terahertz pulses. IEEE J Sel Top Quantum Electron 14(2):505–512
19. Jepsen P, Cooke D, Koch M (2011) Terahertz spectroscopy and imaging – modern techniques and applications. Laser Photonics Rev 5(1):124–166
20. Brown NP (2020) Development and evaluation of terahertz time-domain spectroscopy for electric propulsion plasma diagnostics. PhD thesis, Georgia Institute of Technology
21. Jang D, Uhm HS, Jang D, Hur MS, Suk H (2016) Electron density characterization of inductively-coupled argon plasmas by the terahertz time-domain spectroscopy. Plasma Sources Sci Technol 25(6):065008
22. Sun J, Zheng Y, Shi J, Zhao Y, Li Y, Wu D, Cai H, Zhang X, Zhu X, Liu Y, Sun X, Chao Z, Yin H, Lu W, Ding H (2021) Propagation characteristics of terahertz wave in inductively coupled plasma. Opt Express 29(22):35837–35847
23. Brown NP, Steinberg AM, Deibel JA, Walker ML (2019) Terahertz time-domain spectroscopy as an electric propulsion plasma diagnostic. In: In Proceedings of the 36th International Electric Propulsion Conference. University of Vienna, Austria
24. Brown NP, Grauer SJ, Deibel JA, Walker MLR, Steinberg AM (2021) Bayesian framework for thz-tds plasma diagnostics. Opt Express 29(4):4887–4901
25. Brown NP, Eladl MM, Steinberg AM, Deibel JA, Walker MLR (2021) Noninvasive THz-TDS measurements of plasma bounded and optically shielded by Hall thruster wall material. Plasma Sources Sci Technol 30:075027–075037
26. Dietz P, Reeh A, Keil K, Holste K, Probst U, Klar PJ, Volkmar C (2021) Global models for radio-frequency ion thrusters. EPJ Tech Instrum 8(1):10
27. Schäfer M (1971) Plasmadiagnostik und energiebilanzuntersuchung an dem hf-ionentriebwerk rit 10. PhD thesis, Justus-Liebig-Universität Gießen
28. Monterde MP, Haines MG, Dangor AE, Malik AK, Fearn DG (1997) Kaufman-type xenon ion thruster coupling plasma: Langmuir probe measurements. J Phys D Appl Phys 30:842–855
29. Boeuf JP (2017) Tutorial: Physics and modeling of hall thrusters. J Appl Phys 121(1):011101. https://doi.org/10.1063/1.4972269
30. Jin YS, Kim GJ, Jeon SG (2006) Terahertz dielectric properties of polymers. J Korean Phys Soc 49(2):513
31. Howells SC, Schlie LA (1996) Transient terahertz reflection spectroscopy of undoped InSb from 0.1 to 1.1 THz. Appl Phys Lett 69(4):550–552
32. Van Exter M, Grischkowsky D (1990) Carrier dynamics of electrons and holes in moderately doped silicon. Phys Rev B 41(17):12140
33. FORTRAN program, MAGBOLTZ, S.F. Biagi, version 8.9 and higher, Biagi database. https://nl.lxcat.net/contributors/#d6. Accessed 28 May 2023
34. McEachran R, Stauffer A (2014) Momentum transfer cross sections for the heavy noble gases. Eur Phys J D 68(6):2023. https://doi.org/10.1140/epjd/e2014-50166-7. ISSN 1434-6079. COP database. https://nl.lxcat.net/contributors/#d157. Accessed 28 May
35. FORTRAN program, MAGBOLTZ, S.F. Biagi, version 7.1, Biagi database. https://nl.lxcat.net/contributors/#d3. Accessed 28 May 2023
36. Dobkevicius M, Feili D (2016) A coupled performance and thermal model for radio-frequency gridded ion thrusters. Eur Phys J D 70:227
37. Chabert P, Braithwaite N (2011) Physics of Radio-Frequency Plasmas. Cambridge University Press. ISBN 9780511974342
38. Lieberman M, Lichtenberg A (2005) Principles of plasma discharges and materials processing, chap 12. John Wiley & Sons, Ltd., pp 461–489. ISBN 9780471724254
39. Esteves B, Marmuse F, Drag C, Bourdon A, Laguna AA, Chabert P (2022) Charged-particles measurements in low-pressure iodine plasmas used for electric propulsion. Plasma Sources Sci Technol 31(8):085007

Publisher's Note

Springer Nature remains neutral with regard to jurisdictional claims in published maps and institutional affiliations.